

Comparing Implicit Neural Representations and B-Splines for Continuous Function Fitting from Sparse Samples

Hongze Yu¹, Yun Jiang^{2,3}, Jeffrey A. Fessler^{1,2,3},

¹Department of Electrical Engineering and Computer Science, University of Michigan

²Department of Biomedical Engineering, University of Michigan

³Department of Radiology, University of Michigan

February 26, 2026

Abstract

Continuous signal representations are naturally suited for inverse problems, such as magnetic resonance imaging (MRI) and computed tomography, because the measurements depend on an underlying physically continuous signal. While classical methods rely on predefined analytical bases like B-splines, implicit neural representations (INRs) have emerged as a powerful alternative that use coordinate-based networks to parameterize continuous functions with implicitly defined bases. Despite their empirical success, direct comparisons of their intrinsic representation capabilities with conventional models remain limited. This preliminary empirical study compares a positional-encoded INR with a cubic B-spline model for continuous function fitting from sparse random samples, isolating the representation capacity difference by only using coefficient-domain Tikhonov regularization. Results demonstrate that, under oracle hyperparameter selection, the INR achieves a lower normalized root-mean-squared error, yielding sharper edge transitions and fewer oscillatory artifacts than the oracle-tuned B-spline model. Additionally, we show that a practical bilevel optimization framework for INR hyperparameter selection based on measurement data split effectively approximates oracle performance. These findings empirically support the superior representation capacity of INRs for sparse data fitting.

1 Introduction

Continuous signal representations model an unknown function $f(\vec{r})$ using a parametric mapping $f_{\mathbf{c}}(\vec{r})$, where the coefficients \mathbf{c} are estimated from sampled data. The resulting function can be evaluated at arbitrary spatial locations. This approach is naturally suited for inverse problems, such as magnetic resonance imaging (MRI) [1] and computed tomography, because the recorded measurements (k-space samples in MRI and sinograms in tomography) depend on an underlying signal that is physically continuous. Classical formulations typically use approximation spaces defined by analytical bases or kernels, including Fourier expansions, splines, and radial basis functions [2, 3, 4, 5]. Among these, B-splines are a common choice, where $f(\vec{r})$ is represented in a finite-dimensional spline space defined by a set of knots. The knot density balances between the approximation error and the noise sensitivity. In practical applications, the sensing matrix derived from basis functions is often ill-conditioned due to sparse sampling. A standard approach is to regularize the inverse problem with handcrafted smoothness- or sparsity-promoting penalties.

Recent advances in computer graphics and computer vision, especially in neural rendering and view synthesis [6], have boosted the development of various continuous signal representations. Explicit models construct scenes leveraging localized data structures or graphic primitives, such as

interpolated feature grids [7] and 3D splats based on probability distributions [8]. In contrast, implicit models represents the signal as a continuous, differentiable function that can be queried at arbitrary coordinates [9, 6, 10, 11, 12]. Among these, implicit neural representations (INRs) [13] have emerged as a powerful class of continuous parametric models in which a multilayer perceptron (MLP), composed with a positional encoder, maps spatial coordinates \vec{r} directly to signal values. Unlike the predefined analytical bases in conventional methods, the effective basis of an INR is implicitly defined by the neural network architecture and its weights. INRs have become increasingly popular in MRI [14, 15, 16, 17, 18] in tasks such as undersampled reconstruction and super-resolution, where the continuous formulation aligns with the underlying physics of MRI.

Despite their empirical success, few works have directly compared conventional analytical methods (e.g., B-splines) and INRs in terms of their representation capabilities. To address this gap and motivate the use of INRs, this paper compares INRs with B-spline models for continuous function fitting from sparse, randomly sampled data. In this preliminary empirical study, both methods employed Tikhonov regularization on their weights or coefficients, providing a direct comparison of their intrinsic representation capacities, without confounding influence of additional handcrafted regularizers. Furthermore, we investigate hyperparameter selection in this function-fitting task. For B-splines, we perform an oracle search (assuming access to ground truth) to determine the best possible performance. For INRs, we use a practical bilevel optimization approach [17], which relies on a train/validation split only.

The remaining materials are organized as follows. Section II details the problem formulation and the compared methods. Section III describes the experiment settings. Sections IV and V present experiment results and discussions.

2 Methods

2.1 Problem Formulation

Let $f(\vec{r}) : \mathbb{R}^d \rightarrow \mathbb{R}$ denote a continuous target function defined on a spatial domain. We observe N samples at random locations $\{\vec{r}_n\}_{n=1}^N$ with corresponding values $\{y_n\}_{n=1}^N$, where $y_n = f(\vec{r}_n)$. The goal is to recover f on an arbitrary dense evaluation grid $\vec{z} \in \mathbb{R}^{N_{\text{eval}} \times d}$ from the measured vector $\mathbf{y} = (y_1, \dots, y_N)^T$.

2.2 B-Spline Formulation

As a method that is representative of typical predefined spatial basis functions using in solving inverse problems, we investigated cubic B-splines with M uniformly spaced knots per dimension, yielding $M + 2$ basis functions per dimension and $(M + 2)^2$ coefficients for the 2D function approximation using the standard tensor product representation:

$$f_{\mathbf{c}}(\vec{r}) = \sum_{i,j=1}^{M+2} c_{ij} \beta^{(3)}\left(\frac{r_x - \xi_i}{\Delta}\right) \beta^{(3)}\left(\frac{r_y - \eta_j}{\Delta}\right), \quad (1)$$

where Δ is the knot spacing, and $\mathbf{c} \in \mathbb{R}^{(M+2)^2}$ denotes the vectorized coefficients to be computed from \mathbf{y} .

Hence, the Tikhonov regularized B-spline fitting is formulated as:

$$\hat{\mathbf{c}}(\lambda) = \arg \min_{\mathbf{c}} \|\mathbf{y} - \Phi \mathbf{c}\|_2^2 + \lambda \|\mathbf{c}\|_2^2, \quad (2)$$

where Φ is the design matrix (sensing matrix) of B-spline basis functions evaluated at the sample locations. This quadratic cost function has a closed-form minimizer that we compute using Cholesky decomposition

$$\hat{c}(\lambda) = \left(\Phi^\top \Phi + \lambda I \right)^{-1} \Phi^\top \mathbf{y}. \quad (3)$$

2.3 INR Formulation

The INR parameterizes f as a composition of a positional encoder and an MLP decoder:

$$f_{\theta}(\vec{r}) = M_{\theta_{\text{MLP}}}(\gamma_{\theta_{\text{Enc}}}(\vec{r})), \quad (4)$$

where $\gamma_{\theta_{\text{Enc}}} : \mathbb{R}^d \rightarrow \mathbb{R}^{KF}$ is the multiresolution hash encoder with K levels and F features per level, and $M_{\theta_{\text{MLP}}} : \mathbb{R}^{KF} \rightarrow \mathbb{R}$ is the MLP decoder. The network weights θ include both encoder weights θ_{Enc} and decoder weights θ_{MLP} .

The weight-regularized INR fitting is formulated as:

$$\hat{\theta}(\beta) = \arg \min_{\theta} \frac{1}{N} \|\mathbf{y} - f_{\theta}(\mathbf{z})\|_2^2 + \lambda_{\text{Enc}} \|\theta_{\text{Enc}}\|_2^2 + \lambda_{\text{MLP}} \|\theta_{\text{MLP}}\|_2^2, \quad (5)$$

where $\mathbf{z} \in \mathbb{R}^{N \times d}$ denotes the sample locations and $\mathbf{y} \in \mathbb{R}^N$ the corresponding observations. The hyperparameter vector $\beta = (\lambda_{\text{Enc}}, \lambda_{\text{MLP}}, \tau, b)$ includes the regularization strengths for the encoder and MLP weights, learning rate τ and the cross-level resolution scale factor b for the encoder. We use Adam [19] to perform the minimization in (5).

2.4 Oracle Hyperparameter Search for B-Spline

For B-spline fitting, we perform an oracle grid search over the regularization strength λ and number of knots M , selecting the hyperparameters that minimize the normalized root-mean-squared error (NRMSE) on the dense evaluation grid $\tilde{\mathbf{z}}$:

$$\lambda^*, M^* = \arg \min_{\lambda, M} \frac{\|f_{\hat{c}(\lambda, M)}(\tilde{\mathbf{z}}) - f_{\text{true}}(\tilde{\mathbf{z}})\|_2}{\|f_{\text{true}}(\tilde{\mathbf{z}})\|_2}. \quad (6)$$

This oracle search assumes access to the ground truth and serves to bound the achievable performance.

2.5 Bilevel Optimization for INR

In practice, the ground truth is unavailable, and performing an oracle search for a multidimensional hyperparameter vector can be computationally inefficient. Following the self-supervised hyperparameter optimization framework in [17], we split the observed samples into a training set \mathcal{T} and a validation set \mathcal{V} , and performed bilevel optimization for INR:

$$\begin{aligned} \beta^* &= \arg \min_{\beta} \mathcal{L}_{\mathcal{V}}(\hat{\theta}(\beta)), \\ \text{s.t. } \hat{\theta}(\beta) &= \arg \min_{\theta} \mathcal{L}_{\mathcal{T}}(\beta, \theta), \end{aligned} \quad (7)$$

where

$$\mathcal{L}_{\mathcal{V}}(\hat{\theta}(\beta)) = \frac{1}{|\mathcal{V}|} \sum_{n \in \mathcal{V}} \left(y_n - f_{\hat{\theta}(\beta)}(\vec{r}_n) \right)^2, \quad (8)$$

$$\mathcal{L}_{\mathcal{T}}(\beta, \theta) = \frac{1}{|\mathcal{T}|} \sum_{n \in \mathcal{T}} \left(y_n - f_{\theta}(\vec{r}_n) \right)^2 + \lambda_{\text{Enc}} \|\theta_{\text{Enc}}\|_2^2 + \lambda_{\text{MLP}} \|\theta_{\text{MLP}}\|_2^2, \quad (9)$$

and $\beta = (\lambda_{\text{Enc}}, \lambda_{\text{MLP}}, \tau, b)$ includes regularization strengths, learning rate, and encoder scale factor.

After computing β^* via bilevel optimization, we use the optimized β^* for one final round of function fitting using *all* of the samples.

2.6 Oracle Analysis of INR Regularization

To investigate the sensitivity of INR to the weight decay hyperparameters, we performed an oracle grid search over $\lambda_{\text{Enc}}, \lambda_{\text{MLP}}$ while fixing the learning rate τ and encoder scale factor b at their bilevel optimized values. The oracle optimal regularization strengths are:

$$\lambda_{\text{Enc}}^*, \lambda_{\text{MLP}}^* = \arg \min_{\lambda_{\text{Enc}}, \lambda_{\text{MLP}}} \frac{\|f_{\hat{\theta}(\lambda_{\text{Enc}}, \lambda_{\text{MLP}}; \tau, b)}(\tilde{\mathbf{z}}) - f_{\text{true}}(\tilde{\mathbf{z}})\|_2}{\|f_{\text{true}}(\tilde{\mathbf{z}})\|_2}. \quad (10)$$

For the validation loss based criterion, the optimal hyperparameters are selected by minimizing the validation loss:

$$\lambda_{\text{Enc}}^*, \lambda_{\text{MLP}}^* = \arg \min_{\lambda_{\text{Enc}}, \lambda_{\text{MLP}}} \mathcal{L}_{\mathcal{V}}(\hat{\theta}(\lambda_{\text{Enc}}, \lambda_{\text{MLP}}; \tau, b)). \quad (11)$$

We compared four hyperparameter selection approaches: (1) oracle NRMSE with grid search using 100% of samples for INR training, (2) oracle NRMSE with grid search using 80% of samples for training, (3) validation loss with grid search using an 80%/20% train/validation split, and (4) validation loss with Bayesian optimization (bilevel optimization) [17].

2.7 Evaluation Metric

For both methods, we report the NRMSE on the evaluation grid:

$$\text{NRMSE}(\hat{f}) = \frac{\|\hat{f}(\tilde{\mathbf{z}}) - f_{\text{true}}(\tilde{\mathbf{z}})\|_2}{\|f_{\text{true}}(\tilde{\mathbf{z}})\|_2}, \quad (12)$$

where \hat{f} denotes the reconstructed function ($f_{\hat{\mathbf{c}}}$ or $f_{\hat{\theta}}$).

3 Experiments

To compare the representation capacity of INR and B-spline, we fit a 2D rect function:

$$f(x, y) = \text{Rect}\left(x - \frac{3}{2}\right) \text{Rect}\left(y - \frac{3}{2}\right), \quad (13)$$

using $N = 10000$ points sampled uniformly at random on $[0, 3] \times [0, 3]$. Both methods are evaluated on a dense 501×501 uniform grid $\tilde{\mathbf{z}}$ covering $[-0.3, 3.3] \times [-0.3, 3.3]$. Only Tikhonov regularization on weights/coefficients is applied, excluding additional handcrafted regularizers to isolate the representation capacity of each model.

For B-spline fitting, we used cubic B-splines with uniformly spaced knots and performed an oracle grid search over the regularization strength $\log_{10} \lambda \in [-5, 5]$ with step size 0.1 (101 values), and the number of knots $M \in \{5, 10, 15, \dots, 100\}$ (20 values).

For INR, we used the hash-encoded architecture described in [17] with an 80%/20% train/validation split. The bilevel optimization ran 60 upper-level iterations with 2,000 lower-level iterations each to obtain the optimized hyperparameter vector β^* . For the hyperparameter sensitivity analysis, we fixed the learning rate τ and encoder scale factor b at their bilevel optimized values and performed

grid searches over $\log_{10} \lambda_{\text{Enc}} \in [-4, -1]$ and $\log_{10} \lambda_{\text{MLP}} \in [-9, -6]$ matching the bilevel optimization range, each with step size 0.1 (31 values per axis). The grid search was conducted using three selection criteria: oracle NRMSE with 100% training samples, oracle NRMSE with 80% training samples, and validation loss with 80%/20% train/validation split.

4 Results

4.1 B-Spline Results

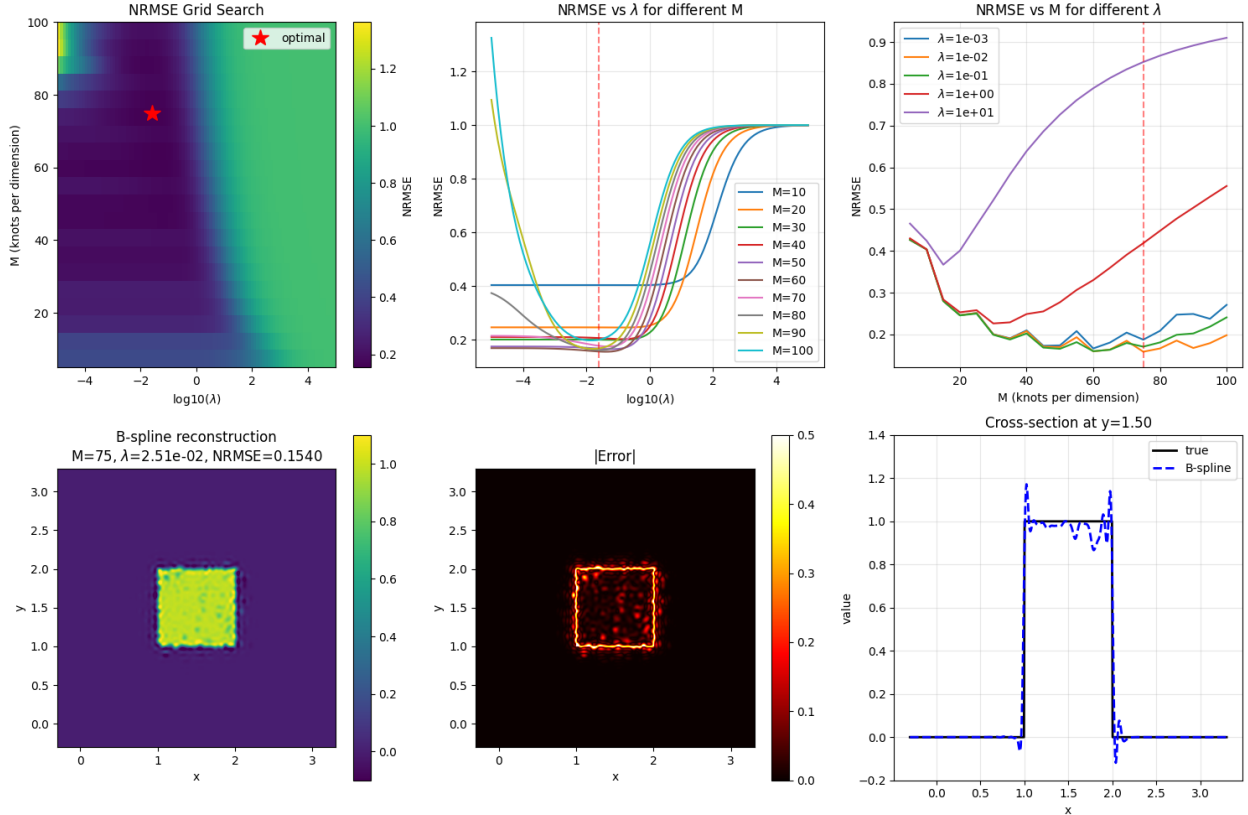


Figure 1: Cubic B-spline fitting with oracle grid search over regularization strength λ and number of knots M . Top row: NRMSE heatmap showing the optimal at $M = 75$, $\lambda = 2.51 \times 10^{-2}$ (red star); NRMSE versus λ for different M ; NRMSE versus M for different λ . Bottom row: optimal reconstruction, absolute error map, and cross-section at $y = 1.50$. The optimal NRMSE is 0.1540.

Fig. 1 shows the B-spline fitting results with oracle grid search over Tikhonov regularization strength λ and number of knots M . The optimal hyperparameter set achieved $\text{NRMSE} = 0.154$ at $M^* = 75$ and $\lambda^* = 2.51 \times 10^{-2}$.

The NRMSE heatmap (top left) and NRMSE vs λ plot (top middle) reveal three different regimes depending on M . For $M < 50$, the B-spline model underfits the data and Tikhonov regularization provides no improvement. For $M \in [50, 80)$, regularization near $\lambda = 10^{-2}$ reduces NRMSE compared to the unregularized case (e.g., by 0.09 for $M = 75$). For $M \geq 80$, the model overfits. While regularization helps, the minimum NRMSE remains higher than the optimal at $M = 75$. The NRMSE versus M curves (top right) further shows that $\lambda \approx 10^{-2}$ consistently

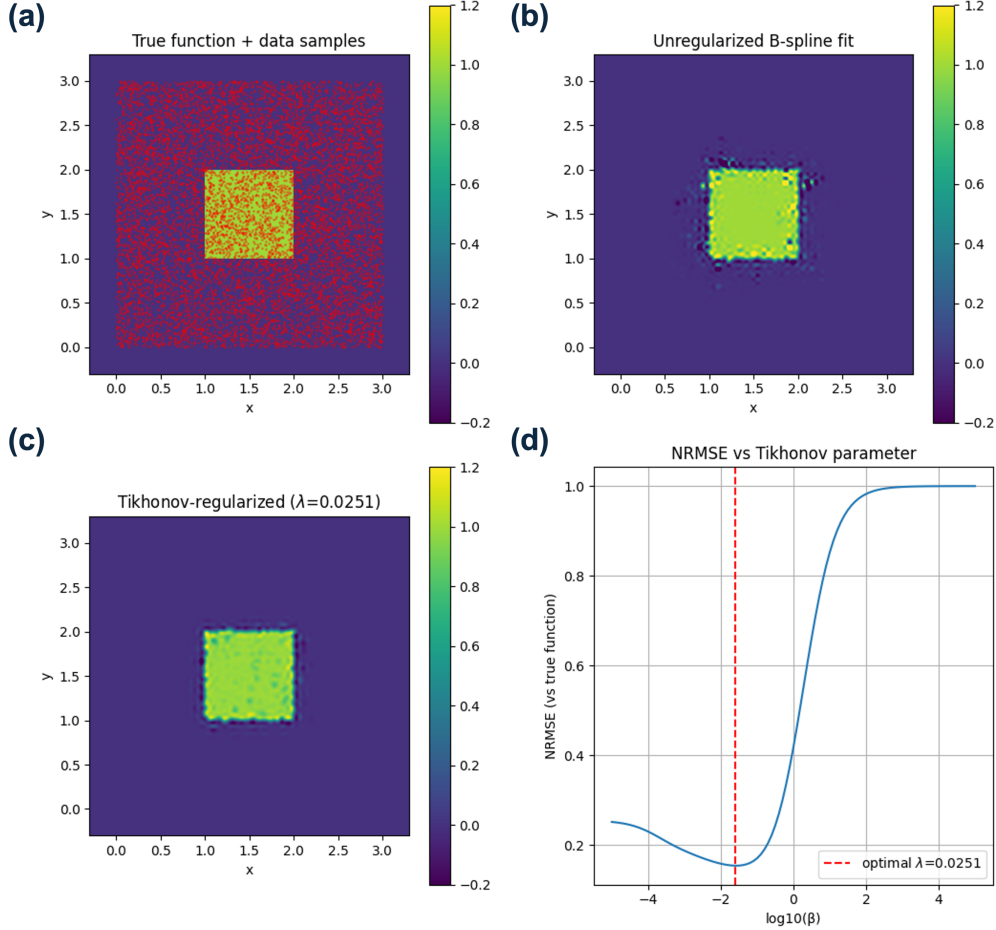


Figure 2: Effect of Tikhonov regularization on cubic B-spline fitting with $M = 75$ knots. (a) True function with random samples. (b) Unregularized fit showing oscillatory artifacts. (c) Optimally regularized fit ($\lambda = 0.0251$) with reduced artifacts but increased blur. (d) NRMSE versus λ , illustrating the bias-variance tradeoff.

produces the lowest error across different knot counts.

Even for the setting that achieved the lowest NRMSE, the optimized B-spline reconstruction (bottom row) exhibits noticeable artifacts near the discontinuities and residual oscillations in the flat-top region, as shown in the cross-section at $y = 1.50$.

Fig. 2 compares the unregularized and optimally regularized B-spline fits at $M = 75$. The unregularized fit (b) shows pronounced oscillatory artifacts near the rectangle edges due to overfitting. Tikhonov regularization (c) suppresses these artifacts but introduces visible blurring. The NRMSE curve (d) shows a general trend of Tikhonov regularization in B-spline fitting: insufficient regularization ($\lambda < 10^{-3}$) results in overfitting, whereas excessive regularization ($\lambda > 10^0$) causes over-smoothing.

4.2 INR Results

Fig. 3 shows the INR hyperparameter sensitivity analysis over the encoder and MLP weight decay parameters (λ_{Enc} , λ_{MLP}). The oracle NRMSE heatmap with 100% training samples (a) yields the optimal weight decay pair $(\lambda_{\text{Enc}}, \lambda_{\text{MLP}}) = (7.94 \times 10^{-3}, 1.00 \times 10^{-6})$. Using 80% training samples

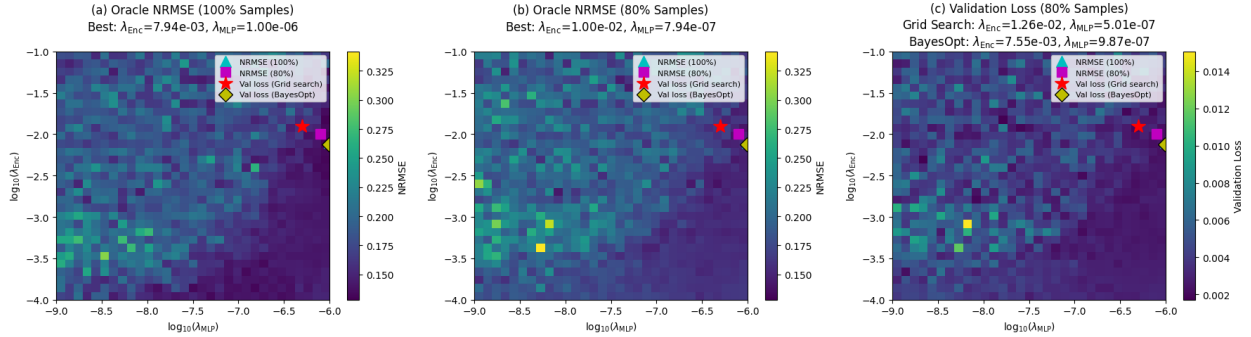


Figure 3: INR hyperparameter sensitivity analysis over encoder and MLP weight decay (λ_{Enc} , λ_{MLP}). (a) Oracle NRMSE with 100% training samples. (b) Oracle NRMSE with 80% training samples. (c) Validation loss with 80%/20% train/validation split. Markers indicate optima: cyan triangle (100% oracle), magenta square (80% oracle), red star (validation grid search), yellow diamond (BayesOpt).

(b) produces a similar optimum at $(1.00 \times 10^{-2}, 7.94 \times 10^{-7})$, indicating that the reduced training set has only a modest effect on the optimal hyperparameters in this task.

When using validation loss as the selection criterion with grid search (c), the optimum shifts to $(1.26 \times 10^{-2}, 5.01 \times 10^{-7})$, which is further from the oracle solution. However, the bilevel optimization scheme using Bayesian optimization (BayesOpt) finds a superior solution at $(7.55 \times 10^{-3}, 9.87 \times 10^{-7})$, closely approximating the oracle optimum despite having no access to the ground truth and limited iterations (60 upper-level iterations compared to 961 grid search evaluations).

Fig. 4 compares INR reconstructions under different hyperparameter selection strategies. Among the four regularized approaches (a–d), oracle grid search with 100% samples achieved the lowest NRMSE of 0.129, representing the best achievable performance. The bilevel optimized INR (d) achieves $\text{NRMSE} = 0.131$, closely matching the oracle and outperforming both the 80% oracle grid search ($\text{NRMSE} = 0.132$) and the validation loss grid search ($\text{NRMSE} = 0.137$). Notably, all four regularized INR results outperformed the optimal B-spline result ($\text{NRMSE} = 0.154$).

Visually, all regularized INR reconstructions exhibit minimal artifacts in the flat-top region of the rectangle, with residual errors mainly appearing near the discontinuities. The cross-section plots at $y = 1.50$ confirm sharper edge transitions and reduced ringing compared to the B-spline results in Fig. 1.

The unregularized INR result in Fig. 4 demonstrates the critical importance of weight regularization for INR. Despite achieving near-zero training loss, the overparameterized nonlinear model severely overfits without regularization, resulting in $\text{NRMSE} = 0.3821$ with pronounced artifacts: underestimation within the rectangle region and spurious oscillations elsewhere. This confirms that, without proper regularization, the expressive capacity of hash-encoded INR leads to poor generalization from sparse samples.

5 Discussion and Conclusions

This work presents preliminary experiments comparing INR and finite-series B-spline representations for continuous function fitting from sparse random samples. Both methods used only Tikhonov regularization on their respective weights/coefficients, isolating the comparison to representation capacity without additional handcrafted priors.

5.1 Comparison of Representation Capacity

The results demonstrate that, under oracle hyperparameter selection, the hash-encoded INR (NRMSE = 0.129) outperformed the cubic B-spline (NRMSE = 0.154) for fitting a 2D rect function. The INR reconstructions exhibited sharper edge transitions and fewer oscillatory artifacts in the flat-top region compared to B-spline, as shown in the cross-section plots.

However, the improved performance comes with tradeoffs. The INR contains substantially more parameters than the B-spline model, making it less parameter-efficient. Additionally, the B-spline formulation is more interpretable, and its NRMSE heatmap is also smoother than the INR heatmaps. The “rougher” INR landscape may be due to the random small weight initialization used for each fit, which introduces the only source of stochasticity in this toy experiment. By contrast, in the MRI reconstruction experiments [17], repeated runs with different initializations produced nearly identical reconstructions, suggesting that weight initialization has a smaller practical impact in that setting. A more thorough theoretical analysis of INR representation and its implicit biases remains an active research direction.

5.2 Effect of Tikhonov Regularization

Both methods benefit from Tikhonov regularization, but the effect differs due to their model differences. For B-spline fitting, regularization directly penalizes coefficient magnitudes, introducing a bias-variance tradeoff where reduced oscillations come at the cost of increased blurring (Fig. 2).

For INR, the encoder-decoder architecture enables a different regularization scheme. Weight penalty on the encoder (λ_{Enc}) directly regularizes the multiresolution feature representation, while the smaller MLP regularization (λ_{MLP}) only mildly constrains the decoded continuous function. The final linear layer can rescale outputs, partially compensating for magnitude shrinkage from regularization of the encoder. This, combined with the much richer nonlinear function class provided by the overparameterized model, may explain why INR achieved lower NRMSE with Tikhonov regularization alone, without requiring additional image-domain priors.

The unregularized INR result (NRMSE = 0.382) further emphasizes the importance of regularization for the overparameterized hash-encoded architecture. Without weight regularization, the model overfit severely despite achieving near-zero training loss.

5.3 Efficacy of Bilevel Optimization

The hyperparameter sensitivity analysis demonstrates that bilevel optimization using Bayesian optimization can effectively approximate oracle performance like the accelerated MRI reconstruction task. The bilevel optimized INR (NRMSE = 0.131) closely matched the 100% oracle result (NRMSE = 0.129) and outperformed validation-based grid search (NRMSE = 0.137), despite operating in continuous hyperparameter space with only 60 upper-level iterations compared to 961 grid search evaluations.

This result supports the use of bilevel optimization for automatic hyperparameter selection when ground truth is unavailable, as is the case in practical MRI reconstruction.

5.4 Conclusions

In summary, this preliminary study provides empirical evidence that hash-encoded INR with Tikhonov regularization can outperform cubic B-spline for fitting discontinuous functions from sparse samples, and that bilevel optimization can effectively select near-optimal hyperparameters without ground truth access. Further study on extending the experiments to more complex tasks,

such as realistic MR reconstruction settings, remains a future direction. It would also be interesting to investigate fitting a smooth function that can be represented perfectly by cubic B-splines.

Acknowledgment

This study was supported in part by NIH grants R37CA263583, R01CA284172, Siemens Healthineers and Cook Medical.

References

- [1] J. A. Fessler, “Model-based image reconstruction for MRI,” *IEEE Signal Process. Mag.*, vol. 27, no. 4, pp. 81–89, 2010.
- [2] G. Wahba, *Spline Models for Observational Data*. SIAM, 1990.
- [3] M. Unser, “Splines: a perfect fit for signal and image processing,” *IEEE Signal Process. Mag.*, vol. 16, no. 6, pp. 22–38, 1999.
- [4] S. Mallat, *A wavelet tour of signal processing*. Academic Press, 1999.
- [5] H. Wendland, *Scattered Data Approximation*. Cambridge: Cambridge University Press, 2005, vol. 17.
- [6] B. Mildenhall, P. P. Srinivasan, M. Tancik, J. T. Barron, R. Ramamoorthi, and R. Ng, “NeRF: Representing scenes as neural radiance fields for view synthesis,” in *Proc. ECCV*, 2020.
- [7] S. Fridovich-Keil, A. Yu, M. Tancik, Q. Chen, B. Recht, and A. Kanazawa, “Plenoxels: Radiance fields without neural networks,” in *Proc. CVPR*, 2022, pp. 5501–5510.
- [8] B. Kerbl, G. Kopanas, T. Leimkühler, and G. Drettakis, “3D Gaussian Splatting for Real-Time Radiance Field Rendering,” *ACM Trans. Graphics*, vol. 42, no. 4, July 2023. [Online]. Available: <https://repo-sam.inria.fr/fungraph/3d-gaussian-splatting/>
- [9] J. J. Park, P. Florence, J. Straub, R. Newcombe, and S. Lovegrove, “DeepSDF: Learning continuous signed distance functions for shape representation,” in *Proc. CVPR*, 2019, pp. 165–174.
- [10] J. T. Barron, B. Mildenhall, M. Tancik, P. Hedman, R. Martin-Brualla, and P. P. Srinivasan, “Mip-NeRF: A multiscale representation for anti-aliasing neural radiance fields,” *ICCV*, 2021.
- [11] T. Müller, A. Evans, C. Schied, and A. Keller, “Instant neural graphics primitives with a multiresolution hash encoding,” *ACM Trans. Graph.*, vol. 41, no. 4, pp. 102:1–102:15, Jul. 2022.
- [12] M. Tancik, P. P. Srinivasan, B. Mildenhall, S. Fridovich-Keil, N. Raghavan, U. Singhal, R. Ramamoorthi, J. T. Barron, and R. Ng, “Fourier features let networks learn high frequency functions in low dimensional domains,” in *Proc. NIPS*, 2020.
- [13] V. Sitzmann, J. N. Martel, A. W. Bergman, D. B. Lindell, and G. Wetzstein, “Implicit neural representations with periodic activation functions,” in *Proc. NIPS*, 2020.

- [14] L. Shen, J. Pauly, and L. Xing, “NeRP: Implicit neural representation learning with prior embedding for sparsely sampled image reconstruction,” *IEEE Trans. Neural Netw. and Learn. Syst.*, vol. 35, no. 1, pp. 770–782, 2024.
- [15] R. Feng, Q. Wu, J. Feng, H. She, C. Liu, Y. Zhang, and H. Wei, “IMJENSE: Scan-specific implicit representation for joint coil sensitivity and image estimation in parallel MRI,” *IEEE Trans. on Med. Imag.*, vol. 43, no. 4, pp. 1539–1553, 2024.
- [16] J. Feng, R. Feng, Q. Wu, X. Shen, L. Chen, X. Li, L. Feng, J. Chen, Z. Zhang, C. Liu, Y. Zhang, and H. Wei, “Spatiotemporal implicit neural representation for unsupervised dynamic MRI reconstruction,” *IEEE Trans. Med. Imag.*, pp. 1–1, 2025.
- [17] H. Yu, J. A. Fessler, and Y. Jiang, “Bilevel optimized implicit neural representation for scan-specific accelerated mri reconstruction,” 2025. [Online]. Available: <https://arxiv.org/abs/2502.21292>
- [18] J. Lyu, L. Ning, W. Consagra, Q. Liu, R. J. Rushmore, B. Bilgic, and Y. Rathi, “Rapid whole brain motion-robust mesoscale in-vivo MR imaging using multi-scale implicit neural representation,” *Med. Imag. Analysis*, vol. 107, p. 103830, 2026.
- [19] D. P. Kingma and J. Ba, “Adam: A method for stochastic optimization,” 2017. [Online]. Available: <https://arxiv.org/abs/1412.6980>

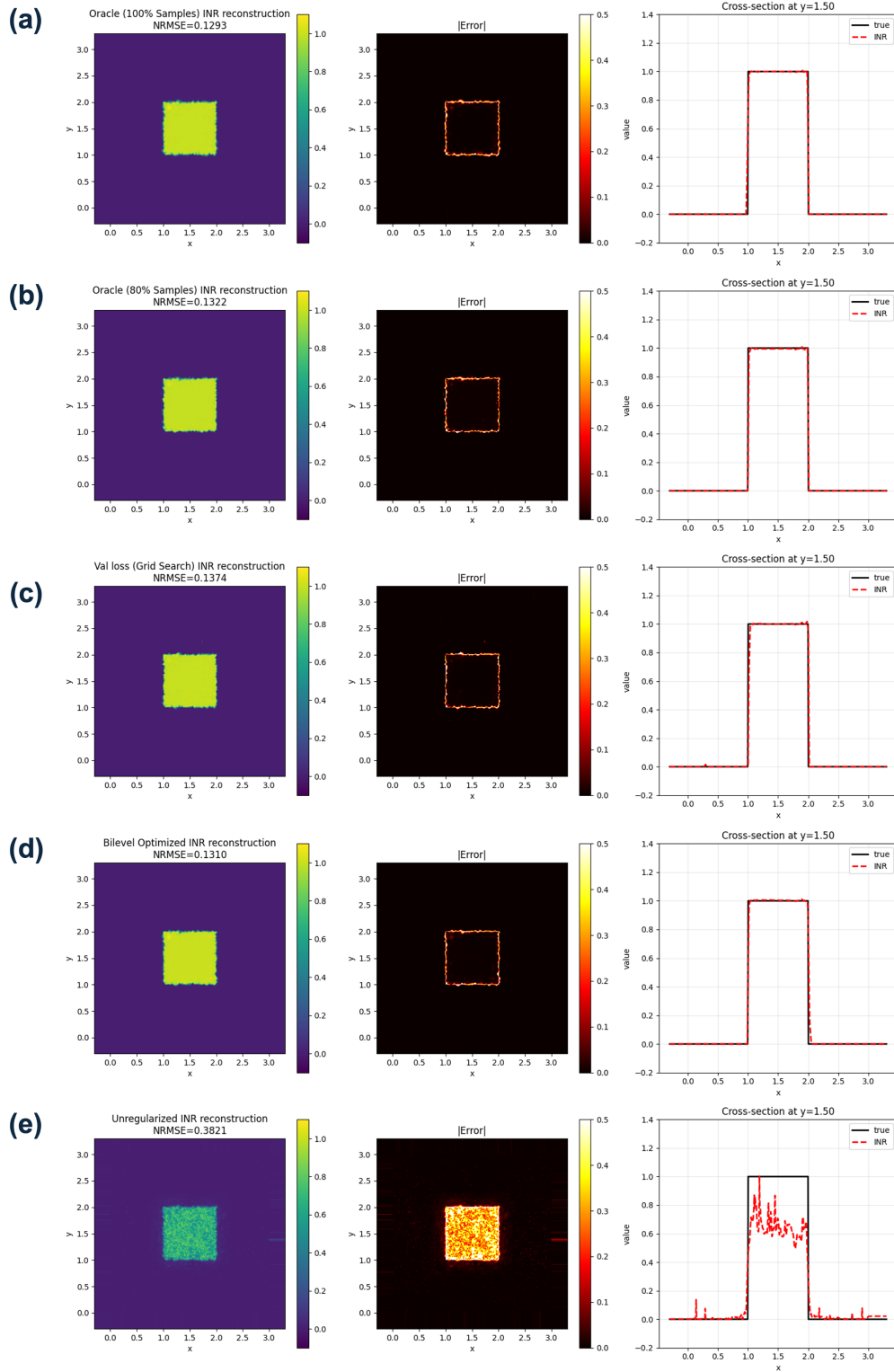


Figure 4: INR reconstruction results under different hyperparameter selection criteria. Each row shows the reconstruction, absolute error map, and cross-section at $y = 1.50$. (a) Oracle grid search with 100% samples (NRMSE = 0.129). (b) Oracle grid search with 80% samples (NRMSE = 0.132). (c) Validation loss grid search with 80%/20% split (NRMSE = 0.137). (d) Bilevel optimization with 80%/20% split (NRMSE = 0.131). (e) Unregularized fitting (NRMSE = 0.382).